https://doi.org/10.3311/PPme.42535

Periodica Polytechnica Mechanical Engineering

Investigating Rotating Noise Sources Using Uniform Circular Arrays: Theoretical Limits and Self-similar Beamforming Maps

Bálint Kocsis[1*], Csaba Horváth[1]

[1] Department of Fluid Mechanics, Faculty of Mechanical Engineering, Budapest University of Technology and Economics, Műegyetem rkp. 3., H-1111 Budapest, Hungary
[*] Corresponding author, e-mail: kocsis.balint@gpk.bme.hu

Received: 21 October 2025, Accepted: 16 December 2025, Published online: 11 January 2026

Abstract

Phased microphone array measurements combined with beamforming signal processing is a widely used approach for localizing and quantifying noise sources, which can be used for turbomachinery applications. Among the various array configurations, uniform circular arrays (UCAs) are frequently employed for rotating sources due to their geometric simplicity and the practical advantage that they can be installed around a free jet or a duct without disturbing the flow. The present article investigates this array design with the aim of providing guidelines for planning proper measurement setups. Particular attention is given to two interdependent parameters: the array diameter and the measurement distance. For a simplified turbomachinery test case, a suitable measurement range is defined within the parameter plane spanned by these variables. The lower and upper bounds of this range are established through the constraints of achieving sufficient spatial resolution and avoiding spatial aliasing, for the estimation of which straightforward formulas are derived herein. Furthermore, it is shown that the parameter plane defined by array diameter and measurement distance can be regarded as the extrusion of one of its cross-sections along specific curves, referred to herein as self-similar curves, as the beamforming maps along these curves are self-similar. This property is advantageous, as conclusions can easily be drawn for the entire parameter space under investigation by carrying out a few simple calculations that utilize the formulas derived herein.

Keywords

beamforming, uniform circular array, array diameter, spatial aliasing, self-similar beamforming curves

1 Introduction

Phased microphone array technology, combined with beamforming signal processing, is a widely used method for localizing and quantifying noise sources. This capability is an important step in the design of quieter machines, which is essential both for health-related reasons and for meeting legislative requirements. Microphone array and beamforming technology can be applied not only to stationary noise sources but also to moving ones, such as those in turbomachinery applications. Localizing noise sources in turbomachinery, however, presents additional challenges. To identify sources associated with rotating components, the rotational motion must be compensated. A widely adopted method for this compensation is the Virtual Rotating Array (VRA) algorithm [1]. The core idea of VRA is to create virtual microphones that rotate synchronously with the turbomachinery, so that the rotating sources appear stationary in the reconstructed sound field. The signals of these virtual microphones are generated through interpolation of the signals from the nearest physical microphones. VRA was originally developed for uniform circular arrays (UCAs), in which microphones are evenly distributed along a circular geometry. In this case, the virtually rotating signals can be obtained by simple linear interpolation between neighboring microphone signals. For technical details of the algorithm, the reader is referred to [1]. Since its introduction, VRA has been extended to other array configurations [2–4]. However, the UCA remains one of the most commonly used designs for microphone array measurements. Over just the past three years, numerous studies have employed UCAs, e.g, in [5–11]. In addition to their simple geometry, UCAs offer the important advantage that they can be mounted around free jets without disturbing the flow, or around ducts, when combined with acoustically transparent duct technology [12]. This makes UCAs particularly powerful tools for aeroacoustic investigations. Their possible use could

Cite this article as: Kocsis, B., Horváth, C. "Investigating Rotating Noise Sources Using Uniform Circular Arrays: Theoretical Limits and Self-similar Beamforming Maps", Periodica Polytechnica Mechanical Engineering, 2026. https://doi.org/10.3311/PPme.42535

make invaluable contributions in studies of flow structures in the wakes of pylons, struts, and other mounting elements, blade-tip vortex shedding, and the noise sources of counter-rotating open rotor configurations [13–15].

The UCA design has been widely employed since the early development of sensor arrays. Foundational theoretical work has been established in the fields of antenna arrays and communication technology. Ma and Balanis derived the array factor in spherical coordinates and expressed it in a simplified form using Bessel functions [16, 17]. Pontoppidan further analyzed the occurrence and locations of grating lobes in circular antenna arrays [18]. However, when it comes to designing microphone array setups for turbomachinery applications – particularly when only a limited number of microphones are available – the guidance found in the literature does not provide much practical help. In the work of Lehmann et al. [19], the UCA was examined with respect to the influence of microphone density on the interpolation accuracy of the VRA algorithm. Microphones per wavelength (*mpw*) was introduced as a spatial sampling metric, and the study showed that sampling is insufficient when $mpw < 2$. This requires that, for any pair of adjacent microphones, their angular separation as viewed from the source remains smaller than the angle associated with one wavelength at that distance. In the work of Ocker et al. [20], the required number of microphones is determined based on a modal decomposition of the rotating sound field. The resulting, readily applicable formulas account for the source frequency, rotational speed, and the rotating source radius. This constraint on the number of microphones is particularly important when modal decomposition-based beamforming methods [21] are employed. While maintaining sufficient microphone density and sufficient modal resolution are crucial requirements for obtaining reliable results, they alone do not define the feasible ranges of other fundamental parameters, such as the array diameter and the measurement distance. Establishing such parameter ranges is of particular importance when installation space imposes strict limitations on the measurement setup. Especially when asynchronous measurements are to be performed, where a series of measurements is carried out while varying a given parameter, such as measurement distance or microphone array diameter. Applying asynchronous measurements and combining the beamforming results has proven effective in reducing sidelobes and improving the quality of beamforming maps in turbomachinery applications [22], being most effective when the investigated parameter is varied across the largest range possible.

The present article aims to define the complete range of two fundamental parameters in the setup for turbomachinery noise measurements: the array diameter and its relation to the measurement distance. The interdependent relationship between these parameters is analyzed in Section 2 using a simplified turbomachinery test case. In Section 3, the concept of self-similar curves is discussed. This concept is particularly valuable, as conclusions can easily be drawn for the entire parameter space under investigation by carrying out a few simple calculations that utilize formulas derived herein. In Section 4, the theoretically derived measurement range is validated through numerical simulations. The results show that the proposed formulas provide reliable bounds for the array diameter, which can be applied with confidence in defining suitable ranges for the asynchronous measurement of turbomachinery applications.

2 Constraints of the measurement setup and determination of the theoretical measurement range

When investigating a turbomachinery test case, such as an axial flow fan (see a simplified model in Fig. 1), the measurement results depend on both the rotor characteristics and the parameters of the phased microphone array. Therefore, it is important to select an appropriate microphone array for the specific task. Certain rotor parameters can often be estimated before the measurement. For instance, the number of noise sources is typically related to the number of rotor blades, while the location of these sources is determined by the underlying noise-generation mechanism, often being dominant near the blade

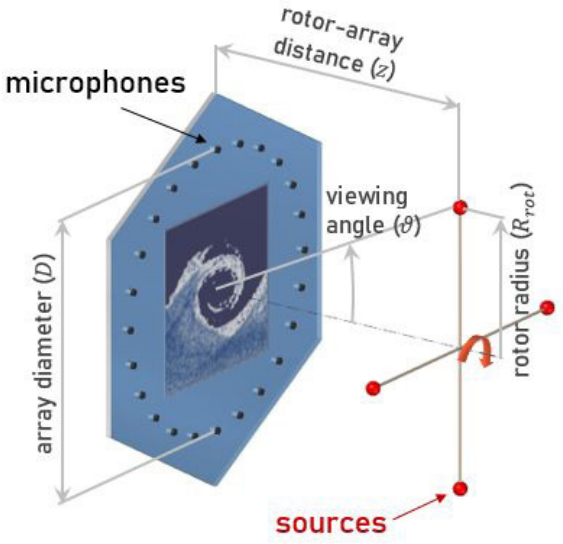

Fig. 1 Simplified model of a turbomachinery test case analyzed using a microphone array

tip radius. The frequency, and hence the wavelength, of the noise sources also depends on the noise-generation mechanism. If the frequency is unknown or a broader range must be investigated, the lower end of the frequency range is usually chosen to satisfy spatial resolution requirements.

As discussed in Section 1, the VRA algorithm employed in this study was originally developed for UCAs [1], which remains a relevant and broadly applied geometry. The present investigation focuses on this microphone array design. In general, a larger number of microphones is desirable to improve beamforming performance; however, equipment is often limited by the number of available sensors or measurement channels. Furthermore, beyond a certain threshold, adding more microphones has little effect on the beamforming results when using a circular arrangement. The required number depends on the noise source frequency, radial position, and rotational speed [19, 20]. The theoretical measurement ranges of the two additional parameters that strongly influence the results, the array diameter D and the rotor-array distance z, are investigated below, and it is shown how their bounds can be determined based on the constraints imposed by spatial resolution and spatial aliasing.

2.1 Bound resulting from the spatial resolution capabilities of a microphone array

Spatial resolution describes the minimum angular separation between two incident waves that allows them to be distinguished. When considering a particular measurement plane, this critical angle can be converted into a corresponding length, allowing spatial resolution to be expressed in length dimensions. For on-axis incidence, the spatial resolution ρ for spatially incoherent incoming waves can be calculated as [23]:

$$\rho = \alpha_R \frac{z}{D} \lambda \tag{1}$$

where λ is the wavelength of the incoming wave, and α_R accounts for the array geometry. For a circular array, according to the Rayleigh criterion, $\alpha_R \cong 1.22$. The Rayleigh criterion is recommended for determining the resolution limit when the beamforming method used is conventional delay-and-sum. If more advanced beamforming techniques are employed – such as DAMAS [24], CLEAN-SC [25], or Functional Beamforming [26] – more demanding resolution criteria, e.g., the Dawes or Sparrow limits [27, 28], may be utilized. The procedure for establishing the lower bound of the array diameter measurement range remains the same in all cases, only the value of α differs. Since the present study uses delay-and-sum beamforming, the lower bound is now formulated based on the Rayleigh limit.

Equation (1) shows the dependence of the spatial resolution on the rotor-array distance, the wavelength (and hence the frequency) of the noise sources, and the array diameter. For a given turbomachinery test case, the minimum required resolution $\rho_{\min}$ can be determined as the distance between the two closest noise sources, i.e., the distance between any pair of neighboring sources. Assuming the sources lie at a radius R_{rot}, and are uniformly distributed with an angular spacing of $2\pi/N$, where N is the total number of sources (see Fig. 2(a)):

$$\rho_{\min} = 2R_{rot} \sin\left(\frac{\pi}{N}\right) \tag{2}$$

Substituting this expression for $\rho_{\min}$ into Eq. (1) and rearranging for D yields a minimum array diameter, denoted $D_{\min}$:

$$D_{\min} = \alpha_R \frac{z}{2R_{rot} \sin\left(\frac{\pi}{N}\right)} \lambda \tag{3}$$

If λ is known, Eq. (3) provides the minimum array diameter necessary to satisfy the resolution requirement for a given rotor-array distance z. In this way, the lower bound of the theoretical measurement range of D is established.

In practical turbomachinery applications, multiple noise generation mechanisms may appear at different radii, or measurements may need to cover a range of frequencies corresponding to the different spectral content of each source. In such cases, each noise generation mechanism should be considered separately. When determining the lower bound of the array diameter, the maximum $D_{\min}$ resulting from the different noise generation mechanisms should be selected to ensure adequate spatial resolution across all sources.

2.2 Bound resulting from spatial aliasing on beamforming maps

Spatial aliasing occurs when false peaks appear on a beamforming map due to insufficient spatial sampling of the

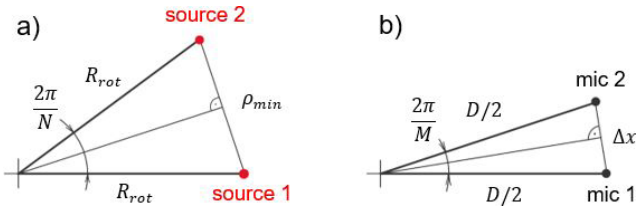

Fig. 2 Schematic illustration of the distance calculation between the (a) sources on the rotor, and (b) the microphones in the array

sound field. These false peaks, also referred to as grating lobes, can have amplitudes equal to or close to that of the true source. They are caused by actual noise sources, however, because the incoming waves are spatially undersampled, these peaks appear at multiple incident angles. According to the Nyquist-Shannon sampling theorem, spatial undersampling can occur when the distance between microphones exceeds half the wavelength of the incoming wave [29]. Spatial aliasing is primarily a concern for regular arrays with periodic microphone arrangements, such as rectangular grid arrays. In contrast, aperiodic arrangements – where microphone spacings vary – can significantly reduce the risk of spatial aliasing. Such aperiodic arrays can be constructed using fewer microphones while still preventing undersampling over a broad frequency range in all directions. Although spatial aliasing may not occur in the strict sense in these cases, inadequate spatial sampling can still produce false peaks. While the amplitudes of these peaks may be lower than those of the true sources, their presence reduces the quality and interpretability of beamforming maps [29]. This phenomenon is presented in Fig. 3(a), which

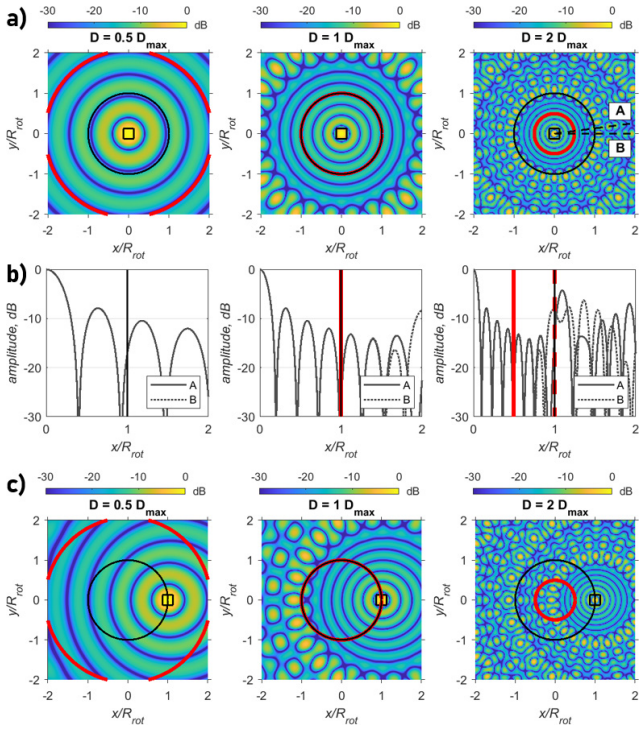

Fig. 3 (a) Array patterns of 24-microphone UCAs, with array diameters indicated above each image. $D_{\max}$ denotes the array diameter where the effects of spatial aliasing appear according to Eq. (8). The black circle marks the rotor's radius, which has been used to define the desired spatial aliasing-free area. The red circle marks the limit of the aliasing-free area. (b) Cross-sections of the array patterns along lines of symmetry A and B, as shown in the right image of the top row. (c) Array patterns with shifted source positions.

shows three array patterns. An array pattern represents the spatial response function of a microphone array, describing its directional sensitivity at a given frequency. In this case, the patterns correspond to plane waves incident perpendicular to the array. The mainlobe (marked by a black square) corresponds to the true source and appears at the center of each image, while the sidelobes correspond to false peaks determined by the microphone arrangement and surround it. The left image shows a case with adequate spatial sampling. The middle image shows the critical state in which aliasing peaks begin to emerge, visible as high amplitudes in the corners of the investigated area. The right image depicts inadequate sampling, where false peaks appear with a maximum amplitude approximately 4 dB lower than the true source. In the figures, the mainlobe is assigned a relative value of 0 dB. Throughout this article, the term spatial aliasing is used to describe the emergence of such false peaks, since their characteristics are consistent with the strict definition of spatial aliasing. To avoid high-amplitude aliasing peaks, it is crucial to ensure adequate spatial sampling, even in aperiodic arrays. In this study, UCAs are investigated. Although the microphone spacings between neighboring microphones of a UCA are equal in magnitude, their directions vary continuously along the perimeter of the circle. Consequently, a circular array can be regarded as aperiodic, despite the regular arrangement of the microphones [30].

As mentioned in Section 1, the behavior of circular arrays has been studied in fields such as antennas and communication technology [16–18]. However, to the authors' best knowledge, no analytical formula exists that precisely describes the location of the innermost ring of spatial aliasing peaks. The array pattern of a circular array can be expressed as an infinite sum of Bessel functions, among which J_1 and J_{-1} contribute most significantly to the inner ring of spatial aliasing peaks [31]. Solving these Bessel functions allows one to locate the spatial aliasing peaks, but the procedure is complex. Here, a new approach is proposed. The authors found that a reasonable estimation can be obtained directly from the Nyquist-Shannon sampling theorem [32]. According to this criterion, spatial aliasing can be avoided if the microphone spacing satisfies:

$$\Delta x < \lambda / 2 \tag{4}$$

When the incoming wave direction deviates from the normal to the array plane, the resulting variations in source–microphone distance across a UCA are not uniform, leading to a non-uniform effective microphone spacing Δx. This variation is not accounted for in the present

analysis, as the authors found that the estimation obtained assuming a uniform Δx agrees well with the spatial-aliasing behavior observed for a UCA. For a direct comparison between a UCA and a truly uniformly spaced linear array, the reader is referred to Appendix A.

According to Eq. (4), the noise source may be located anywhere in front of the array, i.e, for angles $\vartheta < |\pm \pi/2|$, where ϑ is measured from the array center axis (see Fig. 1). For a particular turbomachinery application, the field of view can often be restricted. In such cases, Eq. (4) modifies to:

$$\left|\Delta x \sin\left(\vartheta\right)\right| < \lambda / 2 \tag{5}$$

In the extreme case, the field of view is limited to the angular span of the rotor. Denoting this angle by ϑ_s and assuming the rotor radius R_{rot} is known, the angle depends only on the rotor-array distance z (see Fig. 1):

$$\sin\left(\vartheta_s\right) = \frac{R_{rot}}{\sqrt{z^2 + R_{rot}^2}} = \frac{1}{\sqrt{\left(\frac{z}{R_{rot}}\right)^2 + 1}} \tag{6}$$

For a UCA with M microphones, the spacing between neighboring microphones can be expressed in terms of the array diameter D (see Fig. 2(b)):

$$\Delta x = 2\frac{D}{2}\sin\left(\frac{2\pi}{2M}\right) = D\sin\left(\frac{\pi}{M}\right) \tag{7}$$

Substituting Eqs. (6) and (7) into Eq. (5) yields a constraint on the array diameter D that ensures spatial aliasing is avoided. Equating the left- and right-hand sides and solving for D provides the maximum allowable array diameter $D_{\max}$, which serves as the upper bound of the theoretical measurement range:

$$D_{\max} = \frac{\frac{\lambda}{2}}{\sin\left(\frac{\pi}{M}\right)\frac{1}{\sqrt{\left(\frac{z}{R_{rot}}\right)^2 + 1}}} = \frac{\sqrt{\left(\frac{z}{R_{rot}}\right)^2 + 1}}{2\sin\left(\frac{\pi}{M}\right)}\lambda \tag{8}$$

The results obtained using Eq. (8) are demonstrated in Fig. 3. As described above, the top row shows array patterns for a 24-microphone UCA with varying diameters. The diameters are indicated above each column: the left image shows a diameter being half, and the one on the right shows a diameter being twice $D_{\max}$. The middle image corresponds to when the effects of spatial aliasing appear according to Eq. (8). When $D < D_{\max}$, spatial sampling is sufficient, and the mainlobe is surrounded by smooth, circular sidelobes. At $D = D_{\max}$, peaks begin to appear due to aliasing, while for $D > D_{\max}$, sampling is inadequate, producing distinct, regularly spaced false peaks with lines of symmetry indicated by A and B. Fig. 3(b) shows cross-sections of these array patterns along the lines of symmetry. The black lines denote the rotor radius R_{rot}, which determines the maximum investigation angle ϑ_s. The solid red lines denote the limit of the aliasing-free area using the respective array diameters. At $D = D_{\max}$, the red circle coincides the black one. The dashed red line shows the double of the aliasing limit, where the grating lobes are expected to appear. Over the shown investigation area of 4 R_{rot} × 4 R_{rot}, false peaks due to spatial aliasing emerge as the diameter approaches $D = D_{\max}$, while smaller diameters show no signs of aliasing.

Figs. 3(a) and 3(b) displays an arrangement where the source is located at the center. In turbomachinery, dominant noise sources typically occur along the blade span, often being the most dominant at the blade tip. In such cases, the spatial aliasing peaks shift to the side accordingly, with some part appearing closer to the measurement area. This is illustrated in Fig. 3(c). In the extreme case, the source appears at the blade tip (marked by the black circle). Selecting the array diameter $D_{\max}$ according to Eq. (8) results in the grating lobes approaching the rotor area, as seen in the middle image of Fig. 3(c). When selecting an array diameter $D < D_{\max}$, the grating lobes can be kept outside the rotor area.

In conclusion, Eq. (8) has been derived for circular microphone arrays, starting from the Nyquist-Shannon sampling theorem, and it has been shown that it provides an accurate estimation of the critical array diameter and is adopted hereafter as the upper bound of the theoretical measurement range for D.

2.3 Constraints for the measurement distance

Having established the bounds of the theoretical measurement range for the array diameter D based on spatial resolution and spatial aliasing criteria, it is also necessary to define constraints for the rotor-array distance z. Beamforming techniques are designed to localize sound sources when the array is positioned in the acoustic far-field of the sources. Consequently, ensuring a minimum measurement distance is essential.

For an acoustic monopole, the far-field is typically defined as the distance r at which the product of r and the wavenumber k satisfies $kr >> 1$ (see, e.g., [33]). Substituting the rotor-array distance into this criterion and rearranging yields a simple expression for the lower bound of z:

$$z_{\min} \gg \frac{\lambda}{2\pi} \tag{9}$$

Typical values of kr found in the literature [1, 34] satisfy this criterion, usually exceeding 1 by more than an order of magnitude.

The upper bound of the rotor-array distance z is theoretically limited by the dissipation of the measured sound – that is, when the amplitude decreases to a level comparable with the uncertainty of the microphones. In practice, however, this distance is often large. Large measurement distances require correspondingly large array diameters to maintain sufficient spatial resolution, which may not be feasible given facility constraints. Moreover, the decrease in signal amplitude reduces the signal-to-noise ratio, adversely affecting data quality. For these reasons, the upper bound of z is typically determined by practical considerations rather than theoretical limitations.

2.4 Determination of the theoretical measurement range of the *D* and *z* parameters

As discussed above, the bounds of the theoretical measurement range of D can be defined using the criteria of spatial resolution and spatial aliasing. Combining the expressions obtained in Eqs. (3) and (8), the theoretical range of D can be expressed as:

$$\frac{\alpha_R \dfrac{z}{R_{rot}}}{2\sin\left(\dfrac{\pi}{N}\right)}\lambda < D < \frac{\sqrt{\left(\dfrac{z}{R_{rot}}\right)^2+1}}{2\sin\left(\dfrac{\pi}{M}\right)}\lambda \tag{10}$$

The expressions can be normalized by λ, introducing the dimensionless variables D^* for D/λ and z^* for z/R_{rot}. With this normalization, the bounds become formally independent of the noise source frequency, while z^* represents the ratio of the rotor-array distance and the rotor radius, a characteristic quantity in the measurement setup. Normalization also reduces the number of parameters, yielding:

$$\frac{\alpha_R z^*}{2\sin\left(\dfrac{\pi}{N}\right)} < D^* < \frac{\sqrt{z^{*2}+1}}{2\sin\left(\dfrac{\pi}{M}\right)} \tag{11}$$

Equivalently, this can be written as:

$$D^*_{\min}\left(z^*\right) < D^* < D^*_{\max}\left(z^*\right) \tag{12}$$

The theoretical measurement range of D^* is plotted in Fig. 4 with a green area. The lower bound for z^* is set according to the minimum measurement distance for a source frequency of 4995.7 Hz, the same frequency used in Section 4. For other source frequencies, the minimum measurement distance can be calculated using Eq. (9). The normalized z^*-D^* plane shown in Fig. 4 provides a practical tool for narrowing the number of potential measurement setups. This theoretical range has been applied in the simulation test case discussed in Section 4, where its applicability to rotating noise sources has been investigated. Before proceeding, however, further constraints can be applied to reduce the number of cases that must be investigated.

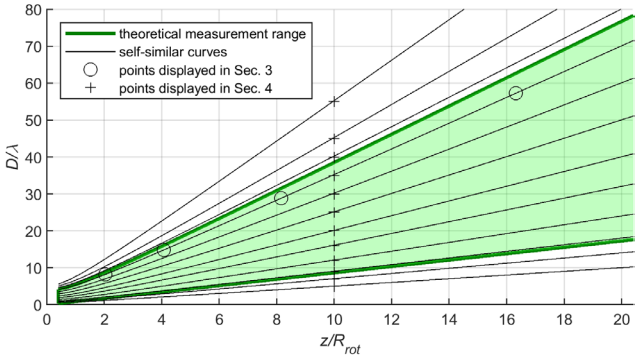

Fig. 4 Definition of the theoretical measurement range in terms of the normalized parameters D^* and z^*

3 Self-similar beamforming map curves on the z^*-D^* parameter plane

Beyond defining the theoretical measurement range of the array diameter and rotor-array distance, an additional important characteristic of the z^*-D^* parameter plane is the similarity of beamforming maps corresponding to different parameter pairs. When the array diameter is varied at a fixed measurement distance (i.e., moving along a vertical line in the parameter plane), the resulting beamforming maps exhibit strong similarity, largely independent of the actual measurement distance. In other words, a beamforming map obtained at one specific z^*-D^* parameter pair can be reproduced in a very similar form at other distances by appropriately adjusting the array diameter. This observation defines a set of curves $D^*(z^*)$ along which the beamforming maps are similar. These will be referred to as self-similar beamforming curves throughout this article. The observed similarity in the acoustic results is connected to the geometrical similarity of the measurement setups. However, because the rotor diameter remains fixed regardless of the chosen distance or array size, the setups are not strictly geometrically similar. Accordingly, the greatest similarity does not occur along a simple line, as would be expected under strict geometrical similarity, but rather along distinct curves. This motivates the definition of self-similar curves through a different approach.

As mentioned in Section 2.2, the array pattern of a UCA can be expressed as an infinite sum of Bessel functions [31]:

$$W\left(\boldsymbol{x}_f,k\right)=\sum_{n=-\infty}^{\infty}J_{nM}\left(k\frac{D}{2}\sin\vartheta\right)e^{inM\left(\frac{\pi}{2}-\varphi\right)} \tag{13}$$

where $\boldsymbol{x}_f$ is the focus gridpoint defined by the angles ϑ and φ (see Fig. 1), k is the wavenumber, M is the number of microphones, and D is the array diameter, and J_{nM} is the Bessel function of the first kind of order $n \cdot M$ where n is the running index. Within the spatial aliasing limits, the array pattern can be well approximated by the zeroth-order Bessel function ($n = 0$) [16], since the neglected terms are several orders smaller. Then Eq. (13) reduces to

$$W\left(\boldsymbol{x}_f,k\right)=J_0\left(k\frac{D}{2}\sin\vartheta\right) \tag{14}$$

Equation (14) implies that if the product $k\ D/2\ \sin\vartheta$ is held constant, the array pattern amplitude remains unchanged. On this basis, self-similar curves can be defined. For a reference pattern obtained with parameters z_{ref} and D_{ref}, one can write (using Eq. 6):

$$k\frac{D}{2}\frac{r}{\sqrt{r^2+z^2}}=k\frac{D_{ref}}{2}\frac{r}{\sqrt{r^2+z_{ref}^2}} \tag{15}$$

Rearranging for D gives:

$$D\left(r,z\right)=\frac{\sqrt{r^2+z^2}}{\sqrt{r^2+z_{ref}^2}}D_{ref} \tag{16}$$

where r is the radius of the focus gridpoint $\boldsymbol{x}_f$, measured from the rotational axis. Using the normalized quantities introduced in Section 2.4, $D^* = D/\lambda$ and $z^* = z/R_{rot}$, Eq. (16) becomes:

$$D^*\left(\frac{r}{R_{rot}},z^*\right)=\frac{\sqrt{\left(\frac{r}{R_{rot}}\right)^2+z^{*2}}}{\sqrt{\left(\frac{r}{R_{rot}}\right)^2+z^{*2}_{ref}}}D^*_{ref} \tag{17}$$

Equation (16) is specific to investigation points at radius r. At the center of the array pattern ($r = 0$), Eq. (16) simplifies to a linear relation:

$$D\left(z\right)=\frac{z}{z_{ref}}D_{ref} \tag{18}$$

A representative curve for the entire investigation area can be obtained by averaging D across focus points within the spatial aliasing limits, where Eq. (14) remains valid. The resulting self-similar curves are dislayed as solid black lines in Fig. 4, closely following the upper theoretical bound given by the right side of Eq. (11), which is explained by their formal similarity. Equation (16) does not depend explicitly on R_{rot}, its effect enters only through the region over which D is averaged. The authors found that, over a broad range of R_{rot}, this approach results in a more accurate representation of the self-similar curves than formulations that account for the off-center source positions.

The self-similar curves are demonstrated through one set of array patterns in Fig. 5 for a reference setup with $D^* = 71.43$ at $z^* = 40.81$. The respective coordinates are indicated above each image and marked as black circles in Fig. 4. In all four cases, the number and distribution of sidelobes are similar, with similarity decreasing somewhat at small distances. This trend is quantified in Fig. 6, where the correlation between the reference and the test array patterns is shown by black circles. The dashed line shows correlation coefficients obtained across a finer scale of distances. Although similarity weakens at small distances, the displayed array patterns remain the closest matches to the reference.

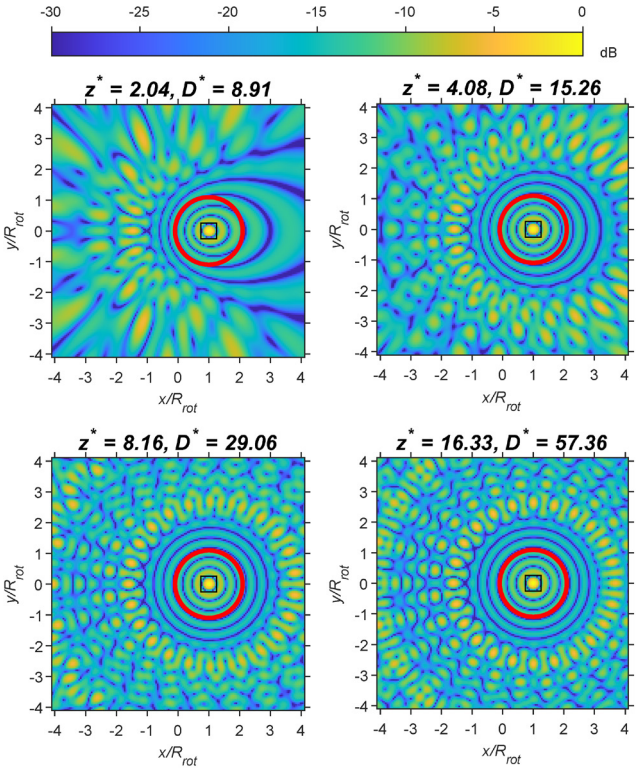

Fig. 5 Set of self-similar beamforming maps, with the corresponding normalized rotor–array distance (z^*) and array diameter (D^*) values indicated above each image

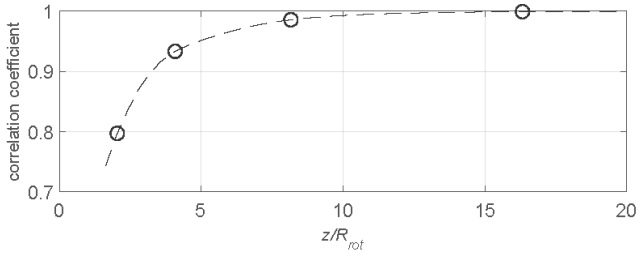

Fig. 6 Correlation coefficient between the self-similar beamforming maps and the reference map (generated at $z^* = 40.81$)

The advantage of the identification of self-similar curves is twofold. First, the array diameter range determined at one measurement distance can be transferred directly to other distances, reducing the number of required investigations in the z^*-D^* plane. This is exploited in Section 4, where results are presented for only one measurement distance. In fact, the transformation need not occur exclusively between two measurement distances, as it may also take place between any two cross-sections of the diagram, as long as the same self-similar curves are intersected.

Second, these curves not only indicate where beamforming maps are similar, but can also be used to assess the extent to which they differ in other directions. Identifying directions associated with stronger variations is important when planning a series of measurements under spatial constraints. This property can be exploited in asynchronous measurements for turbomachinery (as discussed in Section 1), where combining beamforming maps benefits from maximizing differences between the sidelobe arrangements of the individual measurements. Self-similar curves, therefore, identify regions where results resemble one another most closely, providing a basis for selecting alternative configurations that ensure maximum difference in combined analyses.

4 Validation of the theoretical measurement range

Having determined the theoretical measurement range for a UCA, this section investigates the effectiveness of the bound formulas for rotating noise sources.

4.1 Numerical procedure

The simulations in this study have been performed using an in-house beamforming code previously applied in earlier investigations [7, 22]. Four sources have been defined, as shown in Fig. 1, each emitting uncorrelated white noise. The sources have been positioned uniformly around the circumference of a rotor with a diameter of 0.49 m (source positions indicated by black squares and paths by black circles in Fig. 7) rotating at 50 rev/s, resulting in a tangential

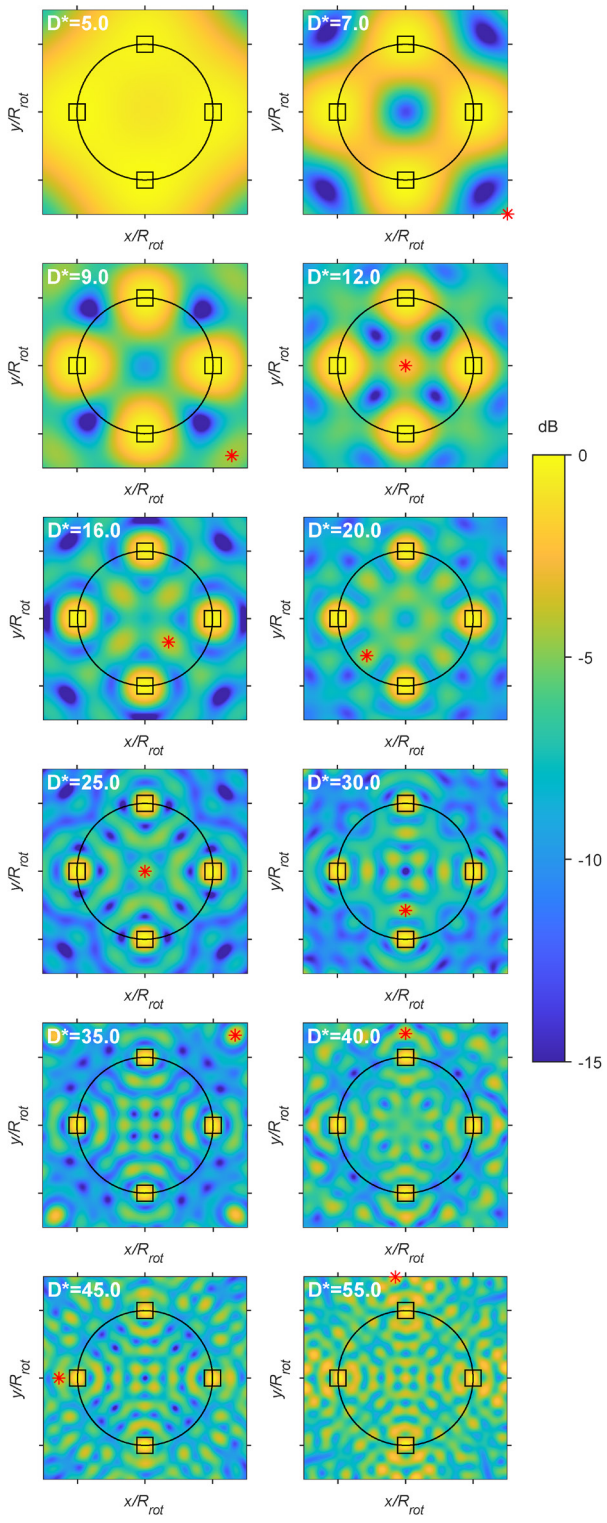

Fig. 7 Beamforming maps for various D^* (specified in the top left corner of each image) at $z^* = 10$, evaluated at the frequency bin 4995.7 Hz. Black squares mark the true source positions, while red asterisks indicate the maximum sidelobe locations

speed of 0.22 Ma at the source positions. The emitted sound has been numerically propagated to the microphones by solving the convected wave equation for a monopole source,

following procedures similar to those reported in the literature [35]. The emission has been oversampled five times relative to the microphone sampling frequency and resampled at the microphones using spline interpolation. The sampling frequency has been 44.1 kHz, and the total sample duration has been 30 s. Beamforming of the rotating noise sources has been performed using the VRA algorithm [1]. Spectra have been computed via averaged FFT, using 1024-point segments with a Hanning window and 50% overlap, resulting in frequency bins of 43.07 Hz bandwidth. The area investigated by beamforming has been defined as 1.5 times the rotor diameter in each direction, using a grid of 121 × 121 points. Although the sources emitted uncorrelated white noise, beamforming maps have been evaluated at a single frequency of 4995.7 Hz for demonstration purposes. Results have been plotted in decibels and normalized to their respective maxima, applying a wide dynamic range of 15 dB. While a narrower dynamic range could enhance the visual separation of the sources, the wider range provides more detailed information on the array's performance.

4.2 Evaluation of the results

As discussed in Section 3, beamforming maps obtained at any specific normalized measurement distance can be transformed to other distances using self-similar curves. Therefore, the simulations performed at a fixed measurement distance can be interpreted for other points along the self-similar curves. In this study, the measurement distance has been set to $z^* = 10$ (10 times the rotor diameter). The rate of change of the beamforming maps with respect to D^* is nonlinear, smaller diameters produce more pronounced changes for the same increment. In order to account for this, D^* values have been selected on a non-uniform scale. The normalized diameters are indicated in Fig. 4 by black crosses, and are also shown in the top-left corner of each image in Fig. 7.

The results are presented in Fig. 7. For the chosen $z^* = 10$, the theoretical bounds for D^* are 8.63 and 38.50. Two diameters below and three above the theoretical range are shown. Below the lower bound, at $D^* = 5$ and 7, the sources are unresolved, producing only a blurred lobe due to insufficient spatial resolution.

At $D^* = 9$, slightly above the lower bound, the sources are clearly separated, with four distinct main lobes corresponding to the source positions (black squares). This separation is maintained throughout the theoretical range up to $D^* = 35$, with high local amplitude maxima marking the sources. The maximum sidelobe level (MSL) is an important measure of array performance. Generally, the MSL is approximately 4 dB below the mainlobe. An exception occurs at $D^* = 12$, where a central sidelobe emerges, reducing the MSL to 2 dB. This results from the superposition of the first sidelobe rings of all four sources at the image center. Until $D^* = 30$, the highest sidelobe is located on the first sidelobe ring of one of the sources. At $D^* = 35$, however, the highest sidelobe shifts to the image corners, and its amplitude increases. This is presented in Fig. 8, where the MSL variation is shown as a function of the array diameter. Black circles indicate the diameters corresponding to Fig. 7, and the dashed line shows the MSL obtained on a finer diameter scale (not presented for brevity). The MSL increases significantly around $D^* = 30$ and remains high for larger diameters. This trend aligns closely with the theoretical upper bound of $D^* = 38.50$. The minor discrepancy arises from two factors. First, the currently investigated area measures 1.5 R_{rot} × 1.5 R_{rot}, whereas in the theoretical definition, it has been restricted to its minimum extent, corresponding to a circle of R_{rot}. The spatial aliasing peaks seen in the corners of Fig. 7 are outside the area applied in the definition. Second, the source position has been chosen at the center in the theoretical definition (indicating an average position for all the sources), whereas now the individual source positions shift the spatial aliasing peaks closer to the center. These differences do not undermine the validity of the upper bound formula, which has reliably estimated the higher end of the measurement range. The authors have had the same experience when investigating other test cases.

For $D^* = 40$, 45, and 55, high MSL values are observed, and source localization becomes increasingly difficult without prior knowledge of their positions. In the extreme case (last image), the highest amplitudes are no longer aligned with the true source positions, demonstrating the destructive effects of spatial aliasing on beamforming maps.

Overall, the lower and upper bound formulas have effectively estimated the usable measurement range. Within

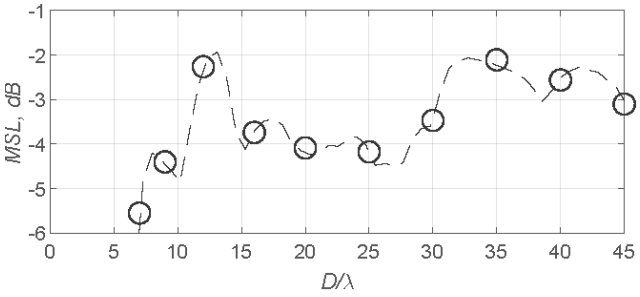

Fig. 8 Variation of the maximum sidelobe level as a function of array diameter

this range, the sources are clearly resolved, and high-amplitude sidelobes due to spatial aliasing do not appear near the rotor area. When the limitations inherent in the definitions are considered, the formulas provide a reliable tool for designing measurement setups involving UCAs for turbomachinery investigations.

5 Conclusions

This article has investigated the application of uniform circular arrays (UCAs), which are frequently employed for turbomachinery noise measurements due to their simple design and their ability to be placed around ducts and free jets. The theoretical measurement range of the array, in terms of the rotor-array distance (z) and the array diameter (D), has been determined for a simplified turbomachinery test case. The lower bound of the array diameter has been established based on the spatial resolution constraint using the Rayleigh criterion, while the upper bound has been determined from the spatial aliasing constraint, and a formula has been proposed to calculate its numerical value. The lower and upper bounds of the rotor-array distance have been defined based on the far-field condition and practical considerations, respectively. The theoretical measurement range has been normalized using the variables z^* and D^*, and the corresponding parameter plane has been visualized in a diagram.

The similarity of the beamforming maps has also been analyzed, allowing the z^*-D^* parameter plane to be simplified through the identification of self-similar beamforming maps along self-similar curves. The points of these curves have been characterized using point spread functions, derived from Bessel function arguments. By employing the concept of self-similar beamforming maps, the results obtained for one set of (z^*, D^*) parameter pairs can be extended to other measurement distances and array diameters, providing an important outcome of the present study.

The validity of the lower- and upper-bound formulas has been demonstrated on a synthetic test case. It has been shown that the theoretical formulas provide a reliable estimate of the usable measurement range. Within the range suggested by the formulas, spatial resolution has been sufficient to separate the noise sources, and spatial aliasing peaks have been effectively excluded from the rotor area. However, it is important to note that at the upper end of the range, spatial aliasing peaks may appear in the corners of the images. To avoid this, a more conservative upper bound can be applied, defining the investigation area larger than the rotor. Considering these limitations, the presented lower- and upper-bound formulas offer practical guidance for engineers designing measurement setups using UCAs for turbomachinery noise analysis.

Acknowledgements

Project no. 143204 has been implemented with the support provided by the Ministry of Innovation and Technology of Hungary from the National Research, Development and Innovation Fund, financed under the OTKA K 22 funding scheme. Project no. TKP-6-6/PALY-2021 has been implemented with the support provided by the Ministry of Culture and Innovation of Hungary from the National Research, Development and Innovation Fund, financed under the TKP2021-NVA funding scheme. This project was supported by the János Bolyai Research Scholarship of the Hungarian Academy of Sciences.

References

[1] Herold, G., Sarradj, E. "Microphone array method for the characterization of rotating sound sources in axial fans", Noise Control Engineering Journal, 63(6), pp. 546–551, 2015. https://doi.org/10.3397/1/376348

[2] Jekosch, S., Sarradj, E. "An Extension of the Virtual Rotating Array Method Using Arbitrary Microphone Configurations for the Localization of Rotating Sound Sources", Acoustics, 2(2), pp. 330–342, 2020. https://doi.org/10.3390/acoustics2020019

[3] Tóth, B., Kalmár-Nagy, T., Vad, J. "Rotating beamforming with uneven microphone placements", In: Proceedings of the 7th Berlin Beamforming Conference, Berlin, Germany, 2018, BeBeC-2018-D23. [online] Available at: http://www.bebec.eu/Downloads/BeBeC2018/Papers/BeBeC-2018-D23.pdf [Accessed: 20 October 2025]

[4] Tóth, B., Vad, J., Kotán, G. "Comparison of the Rotating Source Identifier and the Virtual Rotating Array Method", Periodica Polytechnica Mechanical Engineering, 62(4), pp. 261–268, 2018. https://doi.org/10.3311/PPme.11194

[5] Xu, K., Shi, Y., Qiao, W., Wang, Z. "The Methodological and Experimental Research on the Identification and Localization of Turbomachinery Rotating Sound Source", Energies, 15(22), 8647, 2022. https://doi.org/10.3390/en15228647

[6] Zhao, S., Ma, F. "A circular microphone array with virtual microphones based on acoustics-informed neural networks", Journal of the Acoustical Society of America, 156(1), pp. 405–415, 2024. https://doi.org/10.1121/10.0027915

[7] Lendvai, B., Benedek, T. "Experimental and numerical investigation of the blade tip-related aeroacoustic sound source mechanisms of a ducted low-speed axial flow fan", Applied Acoustics, 215, 109705, 2024. https://doi.org/10.1016/j.apacoust.2023.109705

[8] Kocsis, B., Tokaji, K., Leiber, R., Probst, M., Istók, B., Zhang, H., Pritz, B., Horváth, Cs. "Development of a Measurement methodology for the beamforming investigation of centrifugal fans", In: Proceedings of 10th Berlin Beamforming Conference, Berlin, Germany, 2024, BeBeC-2024-D04. [online] Available at: https://www.bebec.eu/fileadmin/bebec/downloads/bebec-2024/papers/BeBeC-2024-D04.pdf [Accessed: 20 October 2025]

[9] Behn, M., Tapken, U. "Experimental Investigation of Mode-Frequency Scattering at Fan Stages", ASME Journal of Turbomachinery, 146(9), 091010, 2024. https://doi.org/10.1115/1.4065185

[10] Olivieri, M. Bastine, A. Pezzoli, M. Antonacci, F. Abhayapala T., Sarti, A. "Acoustic Imaging With Circular Microphone Array: A New Approach for Sound Field Analysis", IEEE/ACM Transactions on Audio, Speech, and Language Processing, 32, pp. 1750–1761, 2024. https://doi.org/10.1109/TASLP.2024.3369533

[11] Sopranzetti, F., Caputo, A., Castellini, P. "Virtualized Microphone Array for Moving Sources Mapping", Sensors, 25(2), 362, 2025. https://doi.org/10.3390/s25020362

[12] Tokaji, K., Horváth, Cs. "Acoustically transparent duct", International Journal of Aeroacoustics, 17(3), pp. 238–258, 2018. https://doi.org/10.1177/1475472X18763859

[13] Kovács, K. A., Balla, E. "Parameter Identification of the Lagrangian-averaged Vorticity Deviation Vortex Detection Method Through the Investigation of Fluid Flow Around Solid Bodies", Periodica Polytechnica Mechanical Engineering, 67(4), pp. 293–302, 2023. https://doi.org/10.3311/PPme.22874

[14] Lendvai, B., Benedek, T. "Quantifying the Tip Leakage Vortex Wandering in a Low-Speed Axial Flow Fan via URANS Simulation", Periodica Polytechnica Mechanical Engineering, 68(4), pp. 336–345, 2024. https://doi.org/10.3311/PPme.38242

[15] Fenyvesi, B., Horváth, C. "Identification of Turbomachinery Noise Sources via Processing Beamforming Data Using Principal Component Analysis", Periodica Polytechnica Mechanical Engineering, 66(1), pp. 32–50, 2022. https://doi.org/10.3311/PPme.18555

[16] Ma, M. T. "Theory and Application of Antenna Arrays", Wiley, 1974. ISBN 9780471557951

[17] Balanis, C. "Arrays: Linear, planar, and circular", In: Antenna Theory Analysis and Design, Wiley, 2005, pp. 283–384. ISBN 0-471-66782-X

[18] Pontoppidan, K. "Reflector antennas – An overview of surface distortion effects", In: Proceedings of JINA, Nice, France, 1986, pp. 82–93. [online] Available at: https://www.ticra.com/reflector-antennas-overview-surface-distortion-effects/ [Accessed: 20 October 2025]

[19] Lehmann, M., Spehr, C., Schneider, M., Ernst, D. "Investigations on limitations of the virtual rotating array method", In: Proceedings of 8th Berlin Beamforming Conference, Berlin, Germany, 2020, BeBeC-2020-D11. [online] Available at: https://www.bebec.eu/fileadmin/bebec/downloads/bebec-2020/papers/BeBeC-2020-D11.pdf [Accessed: 20 October 2025]

[20] Ocker, C., Herold, G., Krömer, F., Pannert, W., Sarradj, E., Becker, S. "A Comparison of Frequency-Domain Microphone Array Methods for the Characterization of Rotating Broadband Noise Sources", Acta Acustica, 105(1), pp. 66–74, 2019. https://doi.org/10.3813/AAA.919288

[21] Pannert, W., Maier, C. "Rotating beamforming – motion-compensation in the frequency domain and application of high-resolution beamforming algorithms", Journal of Sound and Vibration, 333(7), pp. 1899–1912, 2014. https://doi.org/10.1016/j.jsv.2013.11.031

[22] Kocsis, B., Horváth, Cs. "Further development of rotating beamforming techniques using asynchronous measurements", Journal of Theoretical and Computational Acoustics, 32(1), 2340006, 2024. https://doi.org/10.1142/S2591728523400066

[23] Christensen, J. J., Hald, J. "Beamforming", Brüel & Kjær Technical Review, 2004(1), BV0056, 2004. [online] Available at: https://www.bksv.com/media/doc/bv0056.pdf [Accessed: 20 October 2025]

[24] Brooks, T. F., Humphreys, W. M. "A deconvolution approach for the mapping of acoustic sources (DAMAS) determined from phased microphone arrays", In: Proceedings of the 10th AIAA/CEAS Aeroacoustics Conference, Manchester, UK, 2004, AIAA 2004-2954. https://doi.org/10.2514/6.2004-2954

[25] Sijtsma, P. "CLEAN based on spatial source coherence", International Journal of Aeroacoustics, 6(4), pp. 357–374, 2007. https://doi.org/10.1260/147547207783359459

[26] Dougherty, R. P. "Functional Beamforming for Aeroacoustic Source Distributions", In: Proceedings of the 20th AIAA/CEAS Aeroacoustics Conference, Atlanta, USA, 2014, AIAA 2014-3066. https://doi.org/10.2514/6.2014-3066

[27] Dougherty, R. P., Ramachandran, R. C., Raman, G. "Deconvolution of Sources in Aeroacoustic Images from Phased Microphone Arrays Using Linear Programming", In: Proceedings of the 19th AIAA/CEAS Aeroacoustics Conference, Berlin, Germany, 2013, AIAA 2013-2210. https://doi.org/10.2514/6.2013-2210

[28] Tóth, B., Vad, J. "Algorithmic localisation of noise sources in the tip region of a low-speed axial flow fan", Journal of Sound and Vibration, 393, pp. 425–441, 2017. https://doi.org/10.1016/j.jsv.2017.01.011

[29] Johnson, D. H., Dudgeon, D. E. "Apertures and Arrays", In: Array Signal Processing: Concepts and Techniques, Prentice Hall, 1993, pp. 59–110. ISBN 0130485136

[30] Underbrink, J. R. "Aeroacoustic Phased Array Testing in Low Speed Wind Tunnels", In: Mueller, T. J. (ed.) Aeroacoustic Measurements, Springer, 2002, pp. 98–217. ISBN 9783540417576, https://doi.org/10.1007/978-3-662-05058-3

[31] Manohar, V., Rahmat-Samii, Y. "Revisiting the appearance of grating lobes for antennas with circular periodicity", IEEE Transactions on antennas and propagation, 67(8), pp. 5723–5728, 2019. https://www.doi.org/10.1109/TAP.2019.2920252

[32] Shannon, C. E. "Communication in the Presence of Noise", In: Proceedings of the IRE, 37(1), pp. 10–21, 1949. https://www.doi.org/10.1109/JRPROC.1949.232969

[33] Kinsler, L. E., Frey, A. R., Coppens, A. B., Sanders, J. V. "Fundamentals of Acoustics", Wiley, 1982, pp. 157–159. ISBN 0471029335

[34] Herold, G., Ocker, C., Sarradj, E., Pannert, W. "A Comparison of Microphone Array Methods for the Characterization of Rotating Sound Sources", In: Proceedings of the 7th Berlin Beamforming Conference, Berlin, Germany, 2018. [online] Available at: http://www.bebec.eu/Downloads/BeBeC2018/Papers/BeBeC-2018-D22.pdf [Accessed: 20 October 2025]

[35] Sijtsma, P., Oerlemans, S., Holthusen, H. "Location of rotating sources by phased array measurements", In: Proceedings of 7th AIAA/CEAS Aeroacoustics Conference and Exhibit, Maastricht, Netherlands, 2001. https://doi.org/10.2514/6.2001-2167

Appendix

The spatial aliasing criterion given in Eq. (8) – used in this article to determine the upper bound of the array diameter – describes the aliasing behavior of a uniform linear array (ULA), rather than that of a uniform circular array (UCA). This appendix compares these two sensor arrangements, shown in Fig. A1. The UCA consists of $M = 24$ sensors, matching the configuration used in the main text. For the ULA, the same sensor spacing Δx is applied to ensure that the aliasing characteristics remain identical for both arrays. The resolution of the beamforming results is governed by the characteristic size of the arrays, D and L, respectively (see Fig. A1). To obtain comparable resolution, L was selected to minimize $|(M_{lin} - 1)\Delta x - D|$. With $M_{lin} = 9$, the resulting array length becomes $L = 1.044\ D$. The array patterns were computed for plane waves, using the Eq. (A1) [22]:

$$W\left(\boldsymbol{e}_f\right) = \frac{1}{M}\sum_{m=1}^{M} w_m e^{ik\boldsymbol{e}_f \boldsymbol{x}_m} \tag{A1}$$

where $\boldsymbol{x}_m$ are the microphone coordinates, w_m are the weighting factors (being equally in this investigation), k is the wavenumber defined as $k = 2\pi/\lambda$, where λ is the wavelength, and $\boldsymbol{e}_f$ is the unit vector pointing toward the focus point $\boldsymbol{x}_f$.

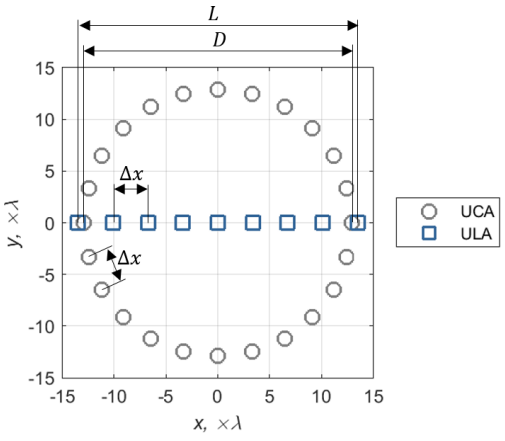

Fig. A1 Microphone arrangements of a uniform linear array (ULA) and a uniform circular array (UCA), having the same sensor spacing and approximately the same characteristic size

The resulting one-dimensional array patterns are shown in Fig. A2. Only the right-hand side is displayed for better visibility. For generality, the array patterns are displayed in terms of $1/2\ k\Delta x \sin\vartheta$, where ϑ is measured from the array's center axis (see Fig. 1). The shown results correspond to $D = 20\lambda$. The ULA pattern is plotted in blue, while the UCA patterns – corresponding to cross-sections A and B in Fig. 3(a)) – are shown in gray. The aliasing limit derived from $\Delta x = \lambda/2$ is marked by solid red lines, and the first grating lobe locations (corresponding to $\Delta x = \lambda$) are indicated by dashed red lines. As seen in Fig. A2, the first grating lobe of the ULA occurs at π. The precise location of the UCA's first grating lobe depends on the number of microphones, but remains close to the ULA's location. In conclusion, the first grating lobe positions are similar for the ULA and UCA. The location of the aliasing limit shows somewhat greater variation: for the ULA it lies at $\pi/2$, beyond which sidelobe peak amplitudes clearly increase, indicating aliasing. For the UCA, the first signs of aliasing appear around 2.1 on the horizontal axis, where cross-sections A and B begin to diverge. This higher value for the UCA could suggest a slightly more relaxed aliasing limit, compared to the ULA. However, for the argument presented in Section 2.2 – specifically, ensuring that aliasing would be prevented even when the source is displaced from the center of the focus plane – Eq. (8) remains as the recommended estimate for the upper bound of the array diameter.

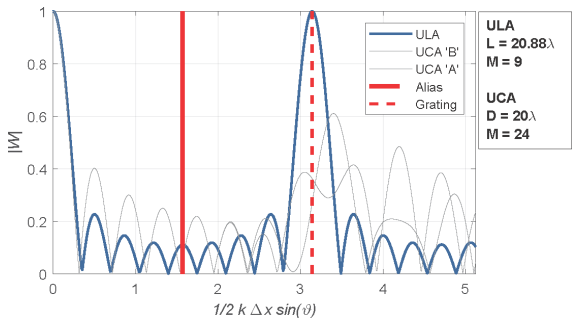

Fig. A2 Array patterns of a ULA and a UCA